The Astrophysical Journal Letters, 944:L27 (12pp), 2023 February 20 https://doi.org/10.3847/2041-8213/acb703

A Strong X-Ray Polarization Signal from the Magnetar 1RXS J170849.0-400910

Silvia Zane[1], Roberto Taverna[2], Denis González–Caniulef[3,4,56], Fabio Muleri[5], Roberto Turolla[1,2], Jeremy Heyl[3], Keisuke Uchiyama[6,7], Mason Ng[8], Toru Tamagawa[6,7,9], Ilaria Caiazzo[10], Niccolò Di Lalla[11], Herman L. Marshall[8], Matteo Bachetti[12], Fabio La Monaca[5], Ephraim Gau[13], Alessandro Di Marco[5], Luca Baldini[14,15], Michela Negro[16,17,18], Nicola Omodei[11], John Rankin[5], Giorgio Matt[19], George G. Pavlov[20], Takao Kitaguchi[9], Henric Krawczynski[13], Fabian Kislat[21], Ruth Kelly[1], Iván Agudo[22], Lucio A. Antonelli[23,24], Wayne H. Baumgartner[25], Ronaldo Bellazzini[14], Stefano Bianchi[19], Stephen D. Bongiorno[25], Raffaella Bonino[26,27], Alessandro Brez[14], Niccolò Bucciantini[28,29,30], Fiamma Capitanio[5], Simone Castellano[14], Elisabetta Cavazzuti[31], Chieng-Ting Chen[25,32], Stefano Ciprini[23,33], Enrico Costa[5], Alessandra De Rosa[5], Ettore Del Monte[5], Laura Di Gesu[31], Immacolata Donnarumma[31], Victor Doroshenko[34], Michal Dovčiak[35], Steven R. Ehlert[25], Teruaki Enoto[9], Yuri Evangelista[5], Sergio Fabiani[5], Riccardo Ferrazzoli[5], Javier A. Garcia[36], Shuichi Gunji[37], Kiyoshi Hayashida[38], Wataru Iwakiri[39], Svetlana G. Jorstad[40,41], Philip Kaaret[25,42], Vladimir Karas[35], Jeffery J. Kolodziejczak[25], Luca Latronico[27], Ioannis Liodakis[43], Simone Maldera[27], Alberto Manfreda[14], Frédéric Marin[44], Andrea Marinucci[31], Alan P. Marscher[40], Francesco Massaro[26,27], Ikuyuki Mitsuishi[45], Tsunefumi Mizuno[46], C.-Y. Ng[47], Stephen L. O'Dell[25], Chiara Oppedisano[27], Alessandro Papitto[24], Abel L. Peirson[11], Matteo Perri[23,24], Melissa Pesce-Rollins[14], Pierre-Olivier Petrucci[48], Maura Pilia[12], Andrea Possenti[12], Juri Poutanen[49], Simonetta Puccetti[23], Brian D. Ramsey[25], Ajay Ratheesh[5], Oliver J. Roberts[25,32], Roger W. Romani[11], Carmelo Sgró[14], Patrick Slane[50], Paolo Soffitta[5], Gloria Spandre[14], Douglas A. Swartz[25,32], Fabrizio Tavecchio[51], Yuzuru Tawara[45], Allyn F. Tennant[25], Nicholas E. Thomas[25], Francesco Tombesi[33,52,53], Alessio Trois[12], Sergey S. Tsygankov[49], Jacco Vink[54], Martin C. Weisskopf[25], Kinwah Wu[1], and Fei Xie[5,55]

[1] Mullard Space Science Laboratory, University College London, Holmbury St Mary, Dorking, Surrey RH5 6NT, UK; s.zane@ucl.ac.uk
[2] Dipartimento di Fisica e Astronomia, Università degli Studi di Padova, Via Marzolo 8, I-35131 Padova, Italy
[3] Department of Physics and Astronomy, University of British Columbia, Vancouver, BC V6T 1Z1, Canada
[4] Institut de Recherche en Astrophysique et Planétologie 9 avenue du Colonel Roche BP 44346, F-31028 Toulouse CEDEX 4 France
[5] INAF Istituto di Astrofisica e Planetologia Spaziali, Via del Fosso del Cavaliere 100, I-00133 Roma, Italy
[6] RIKEN Nishina Center, 2-1 Hirosawa, Wako, Saitama 351-0198, Japan
[7] Department of Physics, Tokyo University of Science, 1-3 Kagurazaka, Shinjuku, Tokyo 162-8601, Japan
[8] MIT Kavli Institute for Astrophysics and Space Research, Massachusetts Institute of Technology, 77 Massachusetts Avenue, Cambridge, MA 02139, USA
[9] RIKEN Cluster for Pioneering Research, 2-1 Hirosawa, Wako, Saitama 351-0198, Japan
[10] Cahill Astrophysics, 1216 California Blvd, MC 350-17, Caltech, Pasadena, CA 91125, USA
[11] Department of Physics and Kavli Institute for Particle Astrophysics and Cosmology, Stanford University, Stanford, CA 94305, USA
[12] INAF Osservatorio Astronomico di Cagliari, Via della Scienza 5, I-09047 Selargius (CA), Italy
[13] Physics Department and McDonnell Center for the Space Sciences, Washington University in St. Louis, St. Louis, MO 63130, USA
[14] Istituto Nazionale di Fisica Nucleare, Sezione di Pisa, Largo B. Pontecorvo 3, I-56127 Pisa, Italy
[15] Dipartimento di Fisica, Universitàdi Pisa, Largo B. Pontecorvo 3, I-56127 Pisa, Italy
[16] University of Maryland, Baltimore County, Baltimore, MD 21250, USA
[17] NASA Goddard Space Flight Center, Greenbelt, MD 20771, USA
[18] Center for Research and Exploration in Space Science and Technology, NASA/GSFC, Greenbelt, MD 20771, USA
[19] Dipartimento di Matematica e Fisica, Università degli Studi Roma Tre, Via della Vasca Navale 84, I-00146 Roma, Italy
[20] Department of Astronomy and Astrophysics, Pennsylvania State University, University Park, PA 16802, USA
[21] University of New Hampshire Department of Physics & Astronomy Space Science Center Morse Hall, Rm 311 8 College Rd Durham, NH 03824, USA
[22] Instituto de Astrofísica de Andalucía-CSIC, Glorieta de la Astronomía s/n, E-18008, Granada, Spain
[23] Space Science Data Center, Agenzia Spaziale Italiana, Via del Politecnico snc, I-00133 Roma, Italy
[24] INAF Osservatorio Astronomico di Roma, Via Frascati 33, I-00078 Monte Porzio Catone (RM), Italy
[25] NASA Marshall Space Flight Center, Huntsville, AL 35812, USA
[26] Dipartimento di Fisica, Università degli Studi di Torino, Via Pietro Giuria 1, I-10125 Torino, Italy
[27] Istituto Nazionale di Fisica Nucleare, Sezione di Torino, Via Pietro Giuria 1, I-10125 Torino, Italy
[28] INAF Osservatorio Astrofisico di Arcetri, Largo Enrico Fermi 5, I-50125 Firenze, Italy
[29] Dipartimento di Fisica e Astronomia, Università degli Studi di Firenze, Via Sansone 1, I-50019 Sesto Fiorentino (FI), Italy
[30] Istituto Nazionale di Fisica Nucleare, Sezione di Firenze, Via Sansone 1, I-50019 Sesto Fiorentino (FI), Italy
[31] Agenzia Spaziale Italiana, Via del Politecnico snc, I-00133 Roma, Italy
[32] Universities Space Research Association (USRA), USA
[33] Istituto Nazionale di Fisica Nucleare, Sezione di Roma Tor Vergata, Via della Ricerca Scientifica 1, I-00133 Roma, Italy
[34] Institut für Astronomie und Astrophysik, Universität Tübingen, Sand 1, D-72076 Tübingen, Germany
[35] Astronomical Institute of the Czech Academy of Sciences, Boční II 1401/1, 14100 Praha 4, Czech Republic
[36] California Institute of Technology, Pasadena, CA 91125, USA
[37] Yamagata University, 1-4-12 Kojirakawa-machi, Yamagata-shi 990-8560, Japan
[38] Osaka University, 1-1 Yamadaoka, Suita, Osaka 565-0871, Japan
[39] International Center for Hadron Astrophysics, Chiba University, Chiba 263-8522, Japan
[40] Institute for Astrophysical Research, Boston University, 725 Commonwealth Avenue, Boston, MA 02215, USA
[41] Department of Astrophysics, St. Petersburg State University, Universitetsky pr. 28, Petrodvoretz, 198504 St. Petersburg, Russia
[42] University of Iowa Department of Physics and Astronomy, Van Allen Hall, 30 N. Dubuque Street, Iowa City, IA 52242, USA
[43] Finnish Centre for Astronomy with ESO, FI-20014 University of Turku, Finland
[44] Université de Strasbourg, CNRS, Observatoire Astronomique de Strasbourg, UMR 7550, F-67000 Strasbourg, France
[45] Graduate School of Science, Division of Particle and Astrophysical Science, Nagoya University, Furo-cho, Chikusa-ku, Nagoya, Aichi 464-8602, Japan
[46] Hiroshima Astrophysical Science Center, Hiroshima University, 1-3-1 Kagamiyama, Higashi-Hiroshima, Hiroshima 739-8526, Japan

[47] Department of Physics, The University of Hong Kong, Pokfulam, Hong Kong
[48] Université Grenoble Alpes, CNRS, IPAG, F-38000 Grenoble, France
[49] Department of Physics and Astronomy, FI-20014 University of Turku, Finland
[50] Center for Astrophysics, Harvard & Smithsonian, 60 Garden Street, Cambridge, MA 02138, USA
[51] INAF Osservatorio Astronomico di Brera, Via E. Bianchi 46, I-23807 Merate (LC), Italy
[52] Dipartimento di Fisica, Università degli Studi di Roma Tor Vergata, Via della Ricerca Scientifica 1, I-00133 Roma, Italy
[53] Department of Astronomy, University of Maryland, College Park, MD 20742, USA
[54] Anton Pannekoek Institute for Astronomy & GRAPPA, University of Amsterdam, Science Park 904, 1098 XH Amsterdam, The Netherlands
[55] Guangxi Key Laboratory for Relativistic Astrophysics, School of Physical Science and Technology, Guangxi University, Nanning 530004, People's Republic of China
Received 2022 December 27; revised 2023 January 23; accepted 2023 January 28; published 2023 February 15

Abstract

Magnetars are the most strongly magnetized neutron stars, and one of the most promising targets for X-ray polarimetric measurements. We present here the first Imaging X-ray Polarimetry Explorer observation of the magnetar 1RXS J170849.0-400910, jointly analyzed with a new Swift observation and archival NICER data. The total (energy- and phase-integrated) emission in the 2–8 keV energy range is linerarly polarized, at a ∼35% level. The phase-averaged polarization signal shows a marked increase with energy, ranging from ∼20% at 2–3 keV up to ∼80% at 6–8 keV, while the polarization angle remains constant. This indicates that radiation is mostly polarized in a single direction. The spectrum is well reproduced by a combination of either two thermal (blackbody) components or a blackbody and a power law. Both the polarization degree and angle also show a variation with the spin phase, and the former is almost anticorrelated with the source counts in the 2–8 and 2–4 keV bands. We discuss the possible implications and interpretations, based on a joint analysis of the spectral, polarization, and pulsation properties of the source. A scenario in which the surface temperature is not homogeneous, with a hotter cap covered by a gaseous atmosphere and a warmer region in a condensed state, provides a satisfactory description of both the phase- and energy-dependent spectro-polarimetric data. The (comparatively) small size of the two emitting regions, required to explain the observed pulsations, does not allow to reach a robust conclusion about the presence of vacuum birefringence effects.

Unified Astronomy Thesaurus concepts: Polarimetry (1278); Magnetars (992)

1. Introduction

The launch of the NASA-Agenzia Spaziale Italiana Imaging X-ray Polarimetry Explorer (IXPE; Weisskopf et al. 2022) in 2021 December opened a new window to our view of the X-ray sky by adding polarimetry to the spectroscopy, timing, and imaging as a tool to interpret astrophysical X-ray sources. IXPE has been in operation for nearly 1 yr now, and already observed more than 30 X-ray sources belonging to different classes.

Particularly interesting for IXPE observations are magnetars, a class of isolated neutron stars (NSs) that are powered by their huge magnetic field (Duncan & Thompson 1992; Thompson & Duncan 1993). They are characterized by an X-ray luminosity $L \approx 10^{31}$–10^{36} erg s^{-1}, spin period $P \approx 1$–12 s, and period derivative $\dot{P} \approx 10^{-13}$–10^{-11} s s^{-1}, implying a dipole field $B \approx 10^{14}$–10^{15} G. Magnetars are extremely active sources over different ranges of luminosities and timescales, from the short-lived X-ray bursts and powerful giant flares to outbursts, during which their persistent X-ray flux suddenly increases by a factor of ≈10–1000 and then gradually decays over months–years (e.g., Rea & Esposito 2011; Coti Zelati et al. 2018).

Magnetar X-ray spectra below 10 keV are typically well reproduced by a two-component model, comprising either two thermal (blackbody, hereafter BB) components or a thermal component plus a nonthermal (power-law, hereafter PL) one. While the BB component(s) is believed to originate from (regions of) the cooling star surface, the PL one is usually interpreted as due to resonant cyclotron scattering (RCS) of thermal photons off magnetospheric currents flowing in a twisted magnetic field. In addition, magnetars exhibit a powerful and highly pulsed nonthermal emission at higher energies, up to ∼100–200 keV, first discovered by International Gamma-Ray Astrophysics Laboratory (INTEGRAL; see, e.g., Turolla et al. 2015; Kaspi & Beloborodov 2017, for reviews).

Strongly magnetized sources, which electromagnetic emission is expected to be highly polarized, are ideal targets for X-ray polarimetry. Emission from highly magnetized NSs is expected to be linearly polarized in two normal modes, the ordinary (O) and extraordinary (X) ones, with the polarization electric vector either parallel or perpendicular to the plane of the photon direction and the (local) magnetic field. The degree of polarization depends on the properties of the emission region, its geometry, magnetic field strength and orientation, and the dominant radiative processes. This makes X-ray polarimetry a new, powerful tool to probe the magnetospheric topology of the magnetar, the state of matter in the star crust, including whether the star has a bare, condensed surface or is surrounded by a gaseous atmosphere (see, e.g., Taverna et al. 2020; Caiazzo et al. 2022, and references therein), and even to test the properties of the QED magnetized vacuum around the star, such as its birefringence (Heyl & Shaviv 2000, 2002).

IXPE first observed a magnetar source, the bright anomalous X-ray pulsar (AXP) 4U 0142 + 61, in 2022 February. The polarization signal was clearly detected at ∼13% level, with both the polarization degree and angle exhibiting a strong dependence on the energy (Taverna et al. 2022). In this paper, we report on the IXPE observation of a second magnetar, the AXP 1RXS J170849.0-400910.

[56] CITA National Fellow.

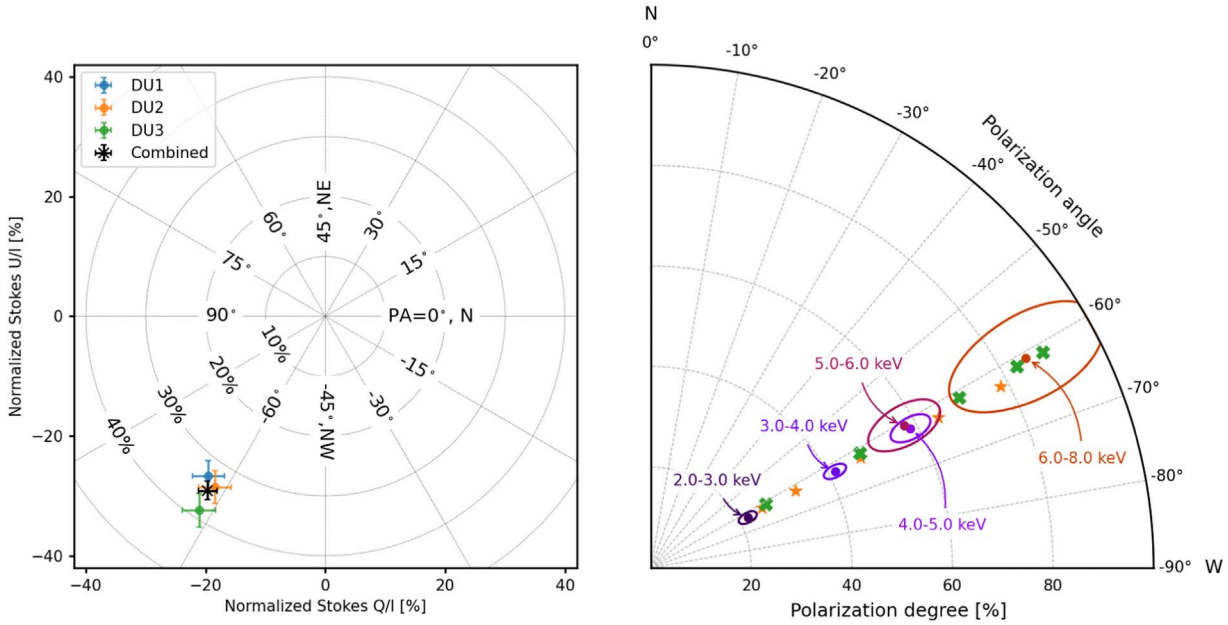

Figure 1. Left: phase- and energy-averaged linear polarization of 1RXS J1708, in terms of the normalized Stokes parameters. Uncertainties are shown at the 68.3% (1σ) confidence level. Circles with center in the origin and increasing radii correspond to increasing values of the polarization degree while different values of the azimuth to different polarization angles. Right: polarization of 1RXS J1708 in different energy bands, computed with IXPEOBSSIM. Contours identify the 50% confidence regions for the joint measurement of the polarization degree and angle (which are not independent variables), accounting for statistical fluctuations only. Orange stars and green crosses show, for the same energy bins, the prediction of the belt+cap and cap+cap models, respectively (see Section 5 for details).

2. Source Properties and Observations

1RXS J170849.0-400910 (1RXS J1708 hereafter) was first identified in the ROSAT All Sky Survey (Voges et al. 1999), but only a few years later, ∼11 s pulsations were discovered by ASCA (Sugizaki et al. 1997). Both the large period derivative ($\dot{P} \sim 2 \times 10^{-11}$ s s^{-1}) and the upper limits inferred for a possible optical counterpart confirmed the source to be a member of the magnetar class (Israel et al. 1999). The value of the period derivative, if interpreted as due to a rotating dipole in vacuum, yields a dipole magnetic field strength of ~ 4–5×10^{14} G. The source presents an erratic timing behavior, characterized by frequent glitching activity that interrupts periods of steady spin-down (Dib & Kaspi 2014). The X-ray spectrum has been fitted with an absorbed BB+PL model, with (slightly variable) photon index $\Gamma \sim 2.6$, and BB temperature $kT \sim 0.45$ keV (Rea et al. 2003, 2007; Krawczynski et al. 2022). The source is radio-quiet. Hard, strongly pulsed X-ray emission extending up to ∼150 keV has been detected from 1RXS J1708 with INTEGRAL (Kuiper et al. 2006); a marked variability in the hardness ratio is also observed (Gotz et al. 2007).

The distance of the source is uncertain. 1RXS J1708 lies in the Galactic plane, and the large column density inferred from X-ray data, $n_{\rm H} \sim 1.36 \times 10^{22}$ cm^{-2}, suggests a distance in the 5–10 kpc range (Israel et al. 1999; Rea et al. 2007), although a smaller value cannot be ruled out, as hinted from spectral fits with atmospheric models or from reddening measures based on Two Micron All Sky Survey stars (Perna et al. 2001; Durant & van Kerkwijk 2006). In this paper, we present the results from the IXPE observation of 1RXS J1708 performed from 2022 September 19 05:08 UTC to 2022 September 29 12:00 UTC and from 2022 September 30 12:52:02 UTC to 2022 October 8 11:17:40 UTC. We complemented the analysis with data from a Swift X-Ray Telescope (XRT; Burrows et al. 2005) target of opportunity observation, performed on 2022 October 20 for a total of 1020 s, and with the most recent NICER (Arzoumanian et al. 2014) data publicly available (see Appendix A for details). Our observations and the methods used for data processing are described in Appendix A.

3. Phase-integrated Polarimetric and Spectropolarimetric Analysis

No variations in either the source or background were found during the two IXPE observations (see Appendix A.1); therefore the combined data are used in the following analysis. The phase-integrated and energy-integrated polarization in the 2.0–8.0 keV interval, which is the nominal IXPE energy range, is shown in Figure 1 (left panel) for each detector unit (DU), and for their combination. The values of the Stokes parameters were derived with the IXPEOBSSIM suite (Baldini et al. 2022),[57] and they are weighted by the (energy-dependent) effective area of the instrument. This allows us to correct the measured polarization, which is convolved with the spectral response of the instrument, and to obtain the polarization of the incoming radiation. The circles and the radial lines in Figure 1 mark the loci of constant polarization degree, PD $= \sqrt{Q^2 + U^2}/I$, and polarization angle, PA $= \arctan(U/Q)/2$, respectively. Since the Stokes parameters are (quasi) normally distributed, we report the one-dimensional uncertainties at 68.3% confidence level (1σ).

The measured polarization angle is ∼60° west of north, and the phase- and energy-integrated polarization degree is remarkably high, ∼35%, that is more than 2.5 times the average X-ray polarization of the only other magnetar observed to date (Taverna et al. 2022).

Even higher polarization degrees are detected by binning the data in five energy intervals, as reported in the right panel of Figure 1; here the contours show the 50% confidence regions in

[57] https://github.com/lucabaldini/ixpeobssim

Table 1
Values of the Measured Polarization Degree and Angle, Obtained with the IXPEOBSSIM Software Suite

	2–3 keV	3–4 keV	4–5 keV	5–6 keV	6–8 keV	2–8 keV
PD—sum [%]	$21.7^{+1.7}_{-1.7}$	$41.3^{+2.0}_{-2.0}$	$58.6^{+3.7}_{-3.7}$	$57.7^{+6.8}_{-6.8}$	85^{+15}_{-15}	$35.1^{+1.6}_{-1.6}$
PD S/N	12.9σ	20.2σ	15.8σ	8.5σ	5.8σ	22.5σ
PA—sum [deg]	$-62.6^{+2.2}_{-2.2}$	$-62.4^{+1.4}_{-1.4}$	$-61.8^{+1.8}_{-1.8}$	$-60.7^{+3.3}_{-3.3}$	$-60.8^{+4.7}_{-4.7}$	$-62.1^{+1.3}_{-1.3}$

Note. Reported values correspond to the sum of the three DUs (the measures of the single DUs are consistent with each other within errors). Uncertainties are obtained at 68.3% confidence level, assuming that the polarization degree and angle are independent. Signal-to-noise ration (S/N) is calculated by dividing the polarization degree obtained by combining the results of the three telescopes on board IXPE by its uncertainty.

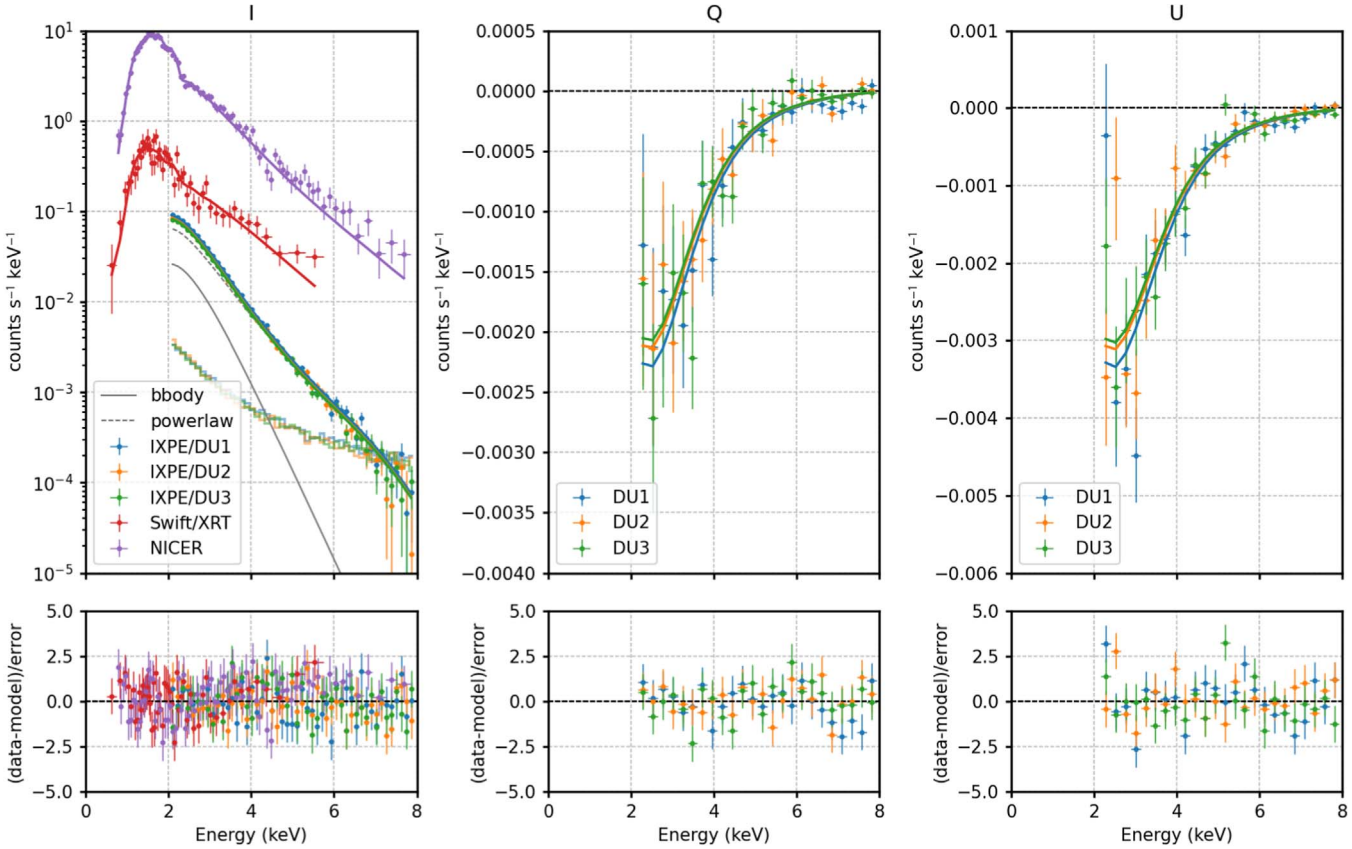

Figure 2. Joint spectropolarimetric fit of IXPE, Swift/XRT, and NICER data. The Stokes I, Q, and U energy spectra are obtained by binning the event-by-event Stokes parameters, calculated following Kislat et al. (2015), according to the measured energy of the event. Q and U are given by the source flux multiplied by the polarization degree and either the cosine or the sine of twice the polarization angle, respectively. The Stokes I, Q, and U energy spectra convolved with the instrument response are shown in the left, central, and right panels, respectively. The best-fit model of the form TBABS*(BBODY * POLCONST + POWERLAW * POLCONST) is shown by the solid lines. Fit residuals are shown in the bottom panels; see Table 2 in Appendix B for the fit parameters. Light colored curves are the background of IXPE detectors.

the polarization degree versus polarization angle plane (see also Table 1). The polarization degree increases from ∼20% between 2 and 3 keV to ∼80% in the 6–8 keV energy range. The polarization angle remains roughly constant in all energy bins.

We performed a spectropolarimetric analysis making use of the IXPE, Swift-XRT, and NICER observations (the latter performed within a month; see Appendix A). We extracted Swift and NICER energy spectra with the standard data analysis tools and used IXPEOBSSIM to derive the IXPE I, Q, and U energy spectra. We use XSPEC (version 12.13.0, Arnaud 1996) for a joint spectropolarimetric fit of the I spectra from all three observatories and the Q and U spectra from *IXPE*.

We tested two models commonly used to interpret magnetar soft X-ray spectra, i.e., an absorbed BB+PL and a BB+BB.[58] We started with the BB+PL model, multiplying the BB and PL components with a polarization factor constant in energy; the corresponding XSPEC model is TBABS*(BBODY * POLCONST + POWERLAW * POLCONST), with abundances from Wilms et al. (2000). We include multiplicative constant factors for each IXPE DU and for each observatory, except for IXPE DU1, which is used as reference. The fit gives a statistically acceptable $\chi^2 = 410.4$ for 408° of freedom (Figure 2). The best-fit parameter values are reported in Table 2 in Appendix B.

[58] Although BB radiation is not polarized, we assume that the shape of the thermal (polarized) spectra can be approximated by the Planck function.

Table 2
Model Parameters for the Joint Spectropolarimetric Fit of IXPE Swift/XRT and NICER Data

Model Parameters	Value	Model Parameters	Value
DU1 normalization	1.0 (frozen)	DU1 normalization	1.0 (frozen)
TBabs nH [10^{22} cm^{-2}]	$2.085^{+0.055}_{-0.050}$	TBabs nH [10^{22} cm^{-2}]	$1.391^{+0.039}_{-0.038}$
kT_{bbody} [keV]	$0.4546^{+0.0077}_{-0.0058}$	kT_{bbody1} [keV]	$0.4354^{+0.0076}_{-0.0078}$
$norm_{bbody}$	$0.0002293^{+0.0000179}_{-0.0000096}$	$norm_{bbody1}$	$0.0005440^{+0.0000097}_{-0.0000091}$
PD_{bbody}	1.0 (U.L.)[a]	PD_{bbody1}	$0.060^{+0.036}_{-0.037}$
PA_{bbody} [deg]	$30.5^{+3.4}_{-3.3}$	PA_{bbody1} [deg]	$-69.0^{+16.7}_{-18.2}$
PowLaw photon index	$2.9672^{+0.0092}_{-0.0567}$	kT_{bbody2} [keV]	$1.073^{+0.031}_{-0.029}$
$norm_{PowLaw}$	$0.04101^{+0.00059}_{-0.00382}$	$norm_{bbody2}$	$0.0002324^{+0.0000082}_{-0.0000079}$
$PD_{powerlaw}$	$0.768^{+0.041}_{-0.040}$	PD_{bbody2}	$0.728^{+0.038}_{-0.037}$
$PA_{powerlaw}$ [deg]	$-60.8^{+1.0}_{-1.2}$	PA_{bbody2} [deg]	$-61.0^{+1.4}_{-1.4}$
DU2 normalization	$0.9567^{+0.0051}_{-0.0049}$	DU2 normalization	$0.9568^{+0.0053}_{-0.0052}$
DU3 normalization	$0.8921^{+0.0048}_{-0.0046}$	DU3 normalization	$0.8922^{+0.0049}_{-0.0049}$
Swift/XRT normalization	$0.922^{+0.032}_{-0.032}$	Swift/XRT normalization	$0.934^{+0.032}_{-0.032}$
NICER normalization	$1.062^{+0.013}_{-0.011}$	NICER normalization	$1.075^{+0.013}_{-0.013}$
χ^2	410.4 with 408 d.o.f.	χ^2	405.8 with 408 d.o.f.
Null prob	45.7%	Null prob	52.2%

Notes. Uncertainties are calculated at the 68.3% confidence level for one parameter of interest. The two leftmost columns refer to the model TBABS*(BBODY * POLCONST + POWERLAW * POLCONST). The normalization of the BB components is defined as L_{39}/D_{10}^2, where L_{39} is the BB luminosity in units of 10^{39} erg s^{-1}, and D_{10} is the distance to the source in units of 10 kpc. The PL normalization is in units of counts keV^{-1} cm^{-2} s^{-1} at 1 keV. The rightmost two columns are for the model TBABS*(BBODY * POLCONST + BBODY * POLCONST).

[a] In this case, the confidence level for the polarization degree of the BB component is not closed, and it was only possible to set an upper limit (U.L.). The value of this parameter is poorly constrained: by freezing the value of PD_{bbody1} to 0.2 also returns an acceptable fit (see the text for details).

Our fit parameters are in approximate agreement with those reported in Rea et al. (2007). The different neutral hydrogen column densities ($n_H \sim 2 \times 10^{22}$ cm^{-2} instead of $\sim 1.4 \times 10^{22}$ cm^{-2}) largely result from the use of a different absorption model and elemental abundances, TBABS and Wilms et al. (2000) in our case instead of PHABS and Anders & Grevesse (1989). We find however a significantly steeper PL than that from Rea et al. (2007). The PL component dominates over the BB component at all energies, the latter contributing only $\sim$20% in the 2–8 keV energy range (see Figure 2).

The simultaneous fit of the Q and U energy spectra provides further insights. We find that the PA associated to the BB component turns out to be different by $\sim 90°$ with respect to that of the PL. This is similar to what IXPE observed in 4U 0142 + 61 (Taverna et al. 2022), and it supports a scenario in which thermal and nonthermal photons are polarized, one in the X and the other in the O mode. The changing polarization degree with energy can be then explained as due to the different relative contributions of the two orthogonally polarized components. However, the polarization degree turns out to be much higher in 1RXS J1708 than that in 4U 0142 + 61. Taken at face value, the best fit gives a 100% polarized BB component (see Table 2 in Appendix B). However, the polarization properties of this component are not well constrained, and for instance, fixing the polarization degree of the BB component to 20% still gives an acceptable fit ($\chi^2 = 434.2$ for 408 degrees of freedom). We infer that the PL component is linearly polarized to $\sim$ 65%–75%, depending on the polarization of the BB component. This polarization degree is much higher than predicted by the resonant scattering scenario (Taverna et al. 2022). It should be noted that the assumptions of constant thermal and PL polarization degrees lead to a significant contribution of the thermal component. The data can be fit with a single PL component if we allow for a polarization degree with a linear energy dependence (we get a $\chi^2 = 454.3$ for 410 degrees of freedom for a PL fit with a photon index of 3.43 ± 0.02); the probability for getting higher χ^2 values by chance is $\sim$6.

In the next step, we fitted the data with an absorbed BB+BB model, again assuming a constant polarization for each additive component; the correspondent XSPEC model is TBABS*(BBODY * POLCONST + BBODY * POLCONST). The result of the fit is shown in Figure 3 (see again Appendix A, Table 2). Also in this case, the fit is acceptable ($\chi^2 = 405.8$ for 408 degrees of freedom), and the high-energy BB component is highly polarized, $\sim$70%. The low-energy component is polarized parallel to the high-energy component. The best-fit model exhibits low polarization in the cold BB component, and by fixing the polarization degree to $\sim$20% also provides an acceptable fit with $\chi^2 = 422.5$ for 409 degrees of freedom. It is worth noting that requiring a low-energy polarization angle orthogonal to the high-energy polarization angle gives a low-energy polarization degree consistent with zero. Therefore, in this scenario, the observed increase of polarization with energy stems from the superposition of two parallel polarized components, a weakly polarized component dominating at low energies and a strongly polarized component dominating at high energies, in the IXPE range.

4. Phase-resolved Spectropolarimetric Analysis

The first step of our phase-resolved analysis involved the determination of an accurate timing solution of the count rate data (see Appendix C). Using epoch MJD 59850.84175 in the Barycentric Dynamical Time (TDB) as a reference, this provided $f = 0.090795742(5)$ Hz, $\dot{f} = -1.87(25) \times 10^{-13}$ Hz s^{-1}. The addition of the second frequency derivative did not improve the fit significantly. We then used this timing solution to perform the phase-resolved analysis. To this aim, we selected photons coming from different rotational phases, and repeated the procedures of Section 3 with the event files of the

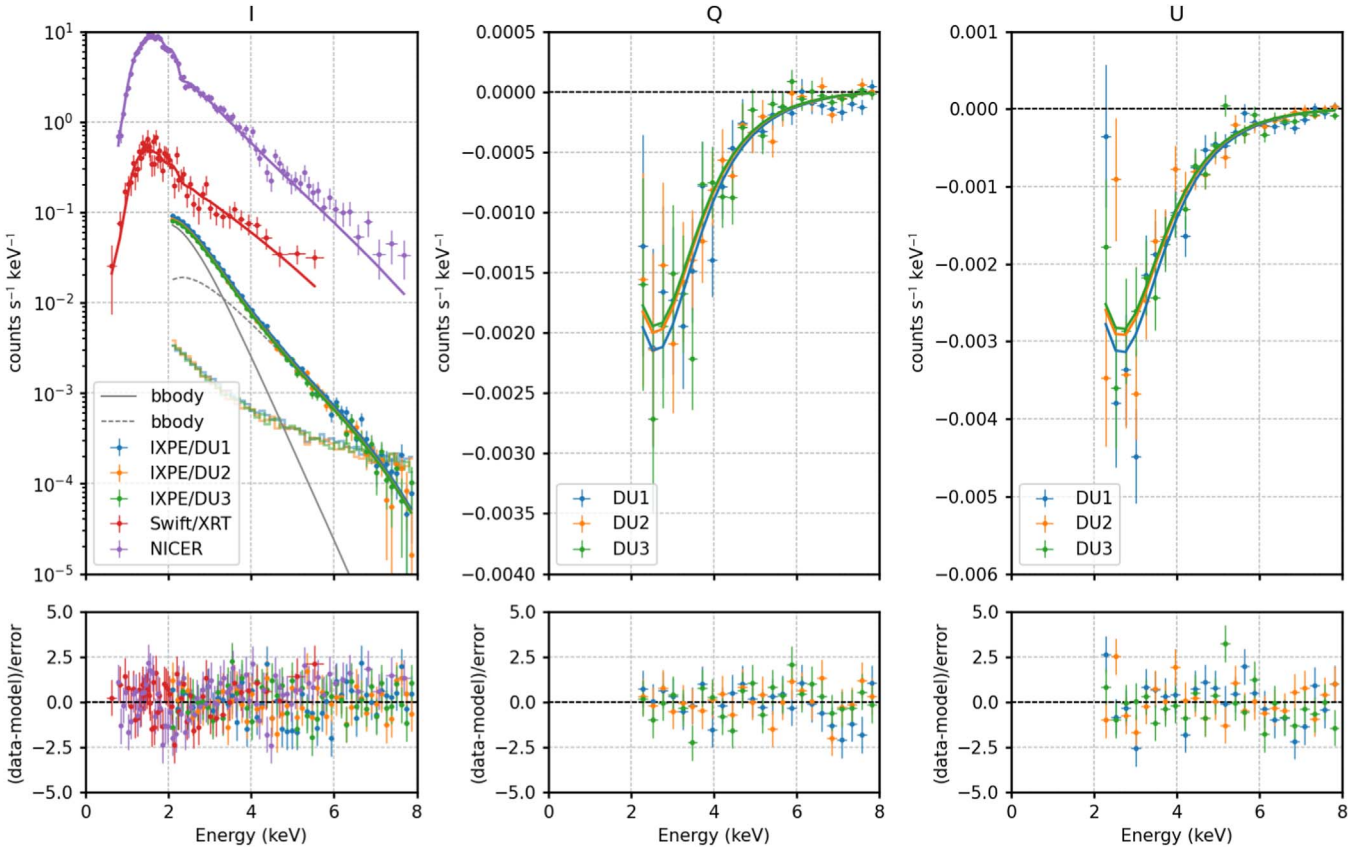

Figure 3. Same as in Figure 2, for the TBABS*(BBODY * POLCONST + BBODY * POLCONST) model. See Table 2 in Appendix B for the fit parameters.

different phase bins. Rotational phases were ascribed to single events starting from their arrival times using the IXPEOBSSIM tool `xpphase`, and the events in the same phase bins were then added together with the tool `xpselect`. Results are shown in Figure 4 for the total (2–8 keV), low (2–4 keV) and high (4–8 keV) energy bands. The source flux exhibits a single-peaked, nearly sinusoidal profile, as already reported by Rea et al. (2003); the pulse shape and the pulsed fraction change with energy. The polarization degree and angle also vary with phase, and their pulse profiles are different in different energy bands. The pulse of the polarization degree is broadly anticorrelated with that of the flux both in the total (2–8 keV) and low (2–4 keV) energy bands.

On the other hand, in the high-energy interval (4–8 keV), the modulation of the signal is less significant, and no robust conclusion can be reached whether this anticorrelation holds at these energies as well.

5. Discussion

1RXS J1708 and the Vela Pulsar Wind Nebula (PWN; Xie et al. 2022) are the most strongly polarized IXPE sources detected so far. The polarization degree of the phase-integrated emission of 1RXS J1708 increases from ∼20% around 2 keV to ∼80% at 7–8 keV. The polarization angle, on the other hand, stays roughly constant at ∼60° (counted west of north). The polarimetric properties of 1RXS J1708 are quite at variance with those of the other magnetar observed by IXPE. For both sources, a BB+PL and a BB+BB model provide a satisfactory fit of the IXPE spectrum (see Section 3). However, 4U 0142 + 61 exhibits a lower polarization degree, which decreases to approximately 0 at ∼5 keV, where the polarization angle swings by 90°, and then increases to ∼35% around 8 keV (Taverna et al. 2022).

The swing of polarization angle by 90° and the presence of a PL tail at higher energies with a value of polarization degree close to 30% led Taverna et al. (2022) to suggest that the X-ray emission from 4U 0142 + 61 is in two different normal modes below and above ∼5 keV. One possibility that has been suggested is that the low-energy photons are mostly polarized in the O mode and come from either a heated equatorial belt on the condensed NS surface or an atmospheric zone that is hit by back-flowing, bombarding magnetospheric currents (Gonzalez-Caniulef et al. 2019), while the high-energy ones are mainly in the X mode being reprocessed by magnetospheric RCS.

The picture for 1RXS J1708 is different. The very high degree of polarization observed at higher energies cannot be reproduced by the RCS mechanism, which indicates that RCS is not present, or, at least, that it does not affect primary photons much in the IXPE energy range. The lack of a swing in the polarization angle points to the emission in the 2–8 keV range being dominated by a single mode. The relative contribution of the other mode is larger at lower energies, explaining the lower polarization degree at lower energies. If we assume that radiation comes from the magnetar surface, a polarization degree as large as ∼70%–80% (as that observed at high energies) can be obtained if the star is covered (at least in part) by an atmosphere (e.g., Gonzalez Caniulef et al. 2016; Taverna et al. 2020; Caiazzo et al. 2022). Emission, then, would be thermal, and so the most likely spectral model, among those compatible with the data (see Section 3), is the BB+BB one. Standard atmospheric emission, however, is hard to reconcile with a polarization degree as low as ∼20% (unless

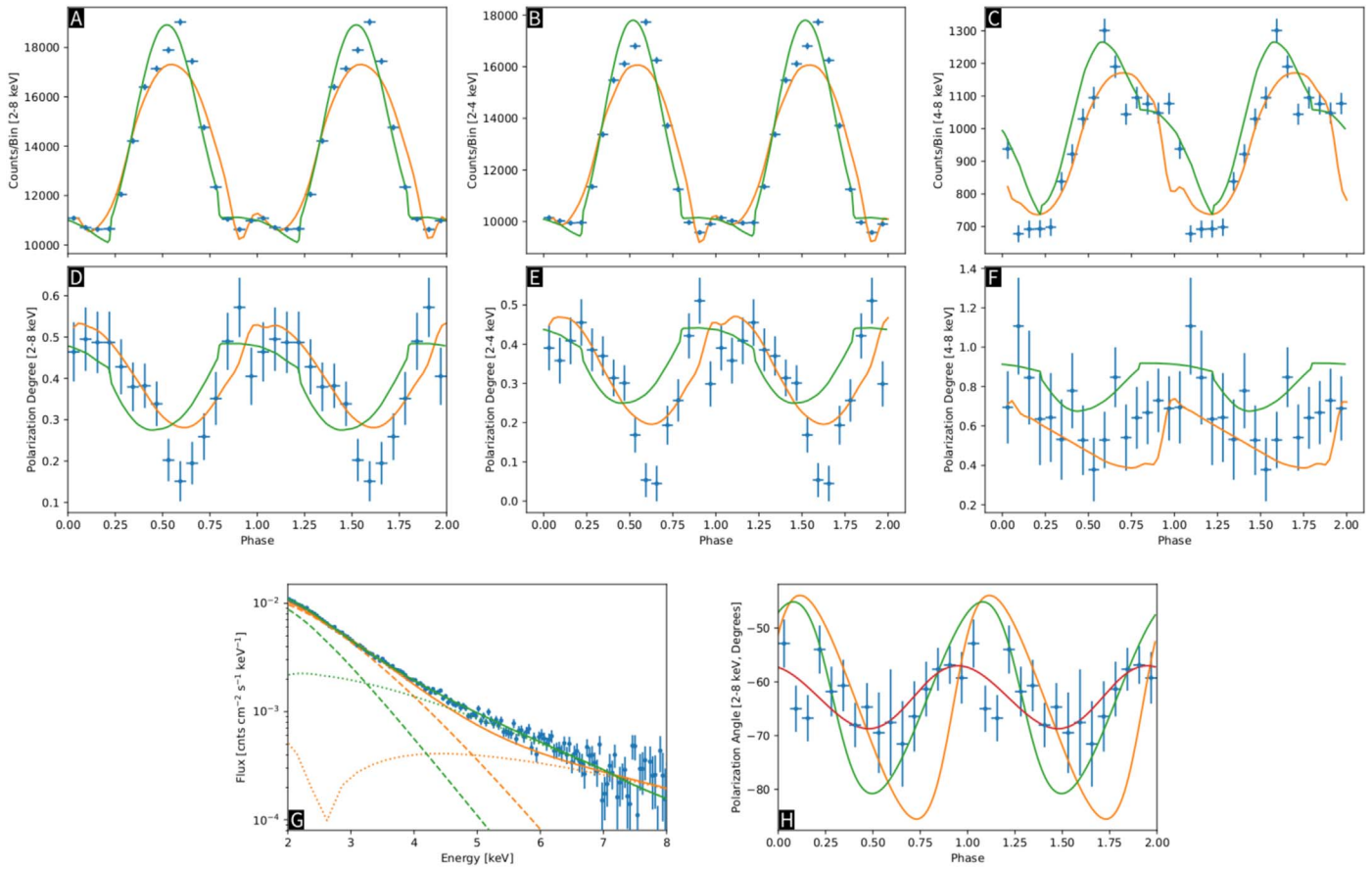

Figure 4. 1RXS J1708 IXPE observation (blue circles with error bars) for the source counts (panels (A)–(C)) and polarization degree (panels (D)–(F)), plotted as a function of the rotational phase (in each row, the three panels from the left to the right show the data integrated over the 2–8, 2–4, and 4–8 keV bands, respectively). Panels (G) and (H) show: (left) the phase averaged spectrum (solid lines) together with the contributions of the condensed zone (dashed lines) and atmospheric zone (dotted lines); (right) the polarization angle as a function of the rotational phase, integrated over the 2–8 keV band. Errors are shown at the 1σ level assuming the polarization degree and polarization angle are not correlated. In all panels, the orange and green lines represent the model expectation within the belt+cap and cap +cap scenarios (solid lines for the total model, dotted and dashed lines in panel (G) only for the two separate components); the red solid line in panel (H) shows the RVM (see the text for the parameter values and other details). Note that data points in the phase-resolved analysis are obtained with IXPEOBSSIM, and therefore independent on the spectral decomposition.

the viewing geometry is very particular), as it is observed in 1RXS J1708 at low energies. It is nevertheless possible that, because of a nonhomogeneous temperature distribution, some regions of the star surface are cold enough to undergo a phase transition that turns the atmosphere into a magnetic condensate. Emission from the condensed surface can be either in the X or in the O mode, but the PD is always modest, $\lesssim$20%, and, if the condensate coexists with a hotter region that has an atmosphere on top, this could explain the IXPE observation of 1RXS J1708.

To explore this scenario, we ran a number of simulations assuming that the star surface comprises a hot atmospheric patch at temperature $T_{\rm hot}$ and a warm condensed region at $T_{\rm warm}$; the rest of the surface is again condensed but at a much colder temperature $T_{\rm cold}$.[59] We tried several different geometries, leaving as free parameters the inclination of the line of sight, χ, and of the magnetic axis, ξ, with respect to the spin axis. This, necessarily oversimplified, picture is mostly meant to suggest possibilities on how the main feature of a complex thermal map may look, and not to provide a diagnostics of the shape and location of the emitting regions.

The emission from the condensate is treated in the free-ion limit and for a Fe composition, following Potekhin et al. (2012). The lack of observed spectral features in the soft X-rays argues against the presence of a heavy-elements atmosphere (see the models by Mori & Ho 2007, for $B = 10^{12}$–10^{13} G). On the other hand, a light elements composition (mostly hydrogen) may be expected if the star experienced episodes of accretion–fallback. We computed emission from a pure hydrogen, completely ionized atmosphere using the numerical setup described in Lloyd (2003).[60] No mode conversion is assumed at the vacuum resonance (see, e.g., Ho & Lai 2003). Photons were then propagated to the observer by using a ray-tracing method. The effects of vacuum birefringence as photons cross the star magnetosphere are accounted for.

We tested various configurations and found that there exist at least two geometrical setups, within the scenario outlined above, that match well most of the observed properties of 1RXS J1708. The first one (model (A), or "belt plus cap") is a variation of the geometry envisaged for 4U 0142 + 61

[59] This was done to ensure a physically consistent picture, and in the actual modeling, $T_{\rm cold} = 0.15$ keV was assumed. However, the contribution of the colder zone does not affect the observed spectral and polarization properties.

[60] We have a caveat that this is an approximation, because strictly speaking these models can be applied only for $B \lesssim 10^{14}$ G.

(Taverna et al. 2022), in which the warm (condensed) region corresponds to an equatorial belt, and the hot (atmospheric) region corresponds to a circular, polar cap; the belt, however, needs to be limited in azimuth in order to reproduce the X-ray pulse profile. In this case, calculations have been performed using the general relativistic ray-tracing code discussed in Zane & Turolla (2006; see also Taverna et al. 2015). In the second model (model (B), or "cap plus cap"), the warm and hot regions are two circular spots, with the warm (condensed) one located about 150° from the spin axis, and a hot (atmospheric) spot located in the opposite hemisphere and displaced in longitude by about 90° with respect to the warm one. For this latter scenario, we used the spectro-polarimetric magnetar model discussed in Caiazzo et al. (2022), properly extended to account for different circular regions. We refer to the original papers for a detailed description of the models and the meaning of the various parameters.

We found that the values of the parameters that best match the data are similar in the two cases: $T_{\rm hot} \sim 0.8$ keV, $T_{\rm warm} \sim 0.6$ keV (all values are referred to the star surface), and a magnetic field of $\sim 10^{14}$ G (model (B)) or $\sim 5 \times 10^{14}$ G (model (A)). Also the values of the geometrical viewing angles are comparable, $\chi \sim 30°$, and $\xi \sim 10°$. The size of the emitting regions turns out to be somewhat smaller for model (B), semiaperture $\sim 5°$ versus $\sim 10°$ for the atmospheric cap and semiaperture $\sim 22°$ of the warm cap as compared to $\sim 30° \times 270°$ of the belt. The observed pulsations require the size of the emitting regions to be relatively small, and this places an upper limit on the source distance to about 5 kpc.

QED vacuum birefringence can strongly affect the polarization properties at infinity, leading to an enhancement in the polarization degree of the observed signal. However, the extent to which QED effects are measurable is actually quite sensitive to the size of the radiating region on the star surface. As discussed in van Adelsberg & Perna (2009), if emission comes from a small polar cap, the depolarization due to geometrical effects is not present, so that the expectations from models computed with or without vacuum birefringence are quite the same. In the case of 1RXS J1708, the small size of the two emitting regions (in particular that of the hot, highly polarized spot) does not allow for a robust test of vacuum birefringence.

Both these models can reproduce the main spectropolarimetric features observed in 1RXS J1708 by IXPE: namely the spectrum; the energy dependence of the phase-averaged polarization degree and angle across the 2–8 keV band (see Figure 1); the pulse profile in the entire IXPE range (2–8 keV), and in the 2–4 and 4–8 keV bands; the energy-integrated polarization degree as a function of phase in the total, 2–4 and 4–8 keV ranges, including the anticorrelation in phase of the polarization degree and the flux in the total and low-energy bands (see Figure 1). As it can be seen in panel (H) of Figure 4, the observed amount of swing in the polarization angle with the phase can also be explained by both models; the red curve depicts the best-fit simple rotating vector model (RVM; with unbinned likelihood analysis, e.g., González-Caniulef et al. 2023). In both the proposed configurations, the model spectra show no features, in agreement with data (see Figure 4). In principle absorption features are expected in the spectrum of a pure hydrogen atmosphere or in that of the magnetic condensate. However, the strong proton cyclotron line in the atmospheric component is ~ 0.6 keV in model (B), and is drowned out by the dominant contribution from the colder belt in model (A). Emission from the condensate component predicts spectral features at low energies (~ 0.6 keV), but at least for these model parameters, they are too faint to be detectable in the currently available spectra.

The observed anticorrelation in the phase of the polarization degree and the flux is due to the relative dominance of two regions, and to the fact that the (less polarized) condensed zone is contributing to much of the counts below ~ 4 keV.

There are, however, some caveats. The surface temperature of the warm condensed region is very close to that of the hotter atmospheric patch. Although the conditions for a phase transition in a strongly magnetized medium are still largely uncertain, assuming a dipolar magnetic field with polar strength $\sim 5 \times 10^{14}$ G, condensation is expected at $T \lesssim 0.5$ and $T \lesssim 0.9$ keV at the equator and the pole, respectively, for a Fe composition (Medin & Lai 2007; see also Figure 1 in Taverna et al. 2020). This may indicate that, if the hot and warm regions at the star surface, which are in different phases, have the same chemical composition, they are very close to the phase transition. Alternatively, it may indicate that the chemical composition varies across the surface (as in our models, which assume a pure hydrogen atmosphere and an iron condensate), that the real surface temperature map is more complicated than what is caught in our, necessarily, oversimplified model, or that there may be departures of the local magnetic field from the (overall) dipole topology.

As mentioned before, the spectro-polarimetric analysis indicates that the data are also compatible with a scenario in which emission is dominated by a nonthermal (PL) component. Would that be the case, the fact that the polarization degree decreases at low energies may be due either to the presence of a second subdominant spectral component with emission in the opposite polarization mode (e.g., a thermal emission from a condensed part of the crust) or to the fact that the nonthermal emission has an intrinsic variation of the polarization properties with energy. The main reason why we have not attempted to explore this scenario is that the very high degree of polarization observed at high energy ($\sim$70%–80%) cannot be reconciled with the physical models commonly proposed to explain the nonthermal emission from magnetars in the soft X-ray band, e.g., RCS (saturated RCS only predicts a $\sim$30% level of polarization). However, it is worth noticing that 1RXS J1708 exhibits a strong nonthermal emission at high energies, as detected in the INTEGRAL band, with extreme variations in phase and energies, whose origin is still unexplained in terms of detailed physical models (Kuiper et al. 2006). It could therefore be possible that this nonthermal component and that observed in the IXPE band could be similar in origin (but with varying degrees of manifestation).

The Imaging X-ray Polarimetry Explorer (IXPE) is a joint US and Italian mission. The US contribution is supported by the National Aeronautics and Space Administration (NASA) and led and managed by its Marshall Space Flight Center (MSFC), with industry partner Ball Aerospace (contract NNM15AA18C). The Italian contribution is supported by the Italian Space Agency (Agenzia Spaziale Italiana; ASI) through contract ASI-OHBI-2017-12-I.0, agreements ASI-INAF-2017-12-H0 and ASI-INFN-2017.13-H0, and its Space Science Data Center (SSDC) with agreements ASI-INAF-2022-14-HH.0 and ASI-INFN 2021-43-HH.0, and by the Istituto Nazionale di Astrofisica (INAF) and the Istituto Nazionale di Fisica

Nucleare (INFN) in Italy. This research used data products provided by the IXPE Team (MSFC, SSDC, INAF, and INFN). We thank K. C. Gendreau and Z. Arzoumanian for their help in scheduling NICER observations of the source. We acknowledge the use of public data from the Swift data archive, and we thank the Swift team for promptly scheduling a target of opportunity (ToO) observation. R.T. and R.T. acknowledge financial support from the Italian Ministry of University and Research (MUR) through grant PRIN 2017LJ39LM. D.G.-C., J.H., and I.C. acknowledge support from the Natural Sciences and Engineer Council of Canada and the Canadian Space Agency. M.N. acknowledges the support by NASA under award number 80GSFC21M0002. T.T. was supported by grant JSPS KAKENHI JP19H05609. H.K. and E.G. acknowledge NASA support under grants 80NSSC18K0264, 80NSSC22K1291, 80NSSC21K1817, and NNX16AC42G. We thank an anonymous referee for a careful reading of the paper.

Facilities: IXPE, Swift (XRT), NICER.

Appendix A
Observational Data and Data Processing

A.1. IXPE

IXPE observed 1RXS J1708 in two segments close in time, from 2022 September 19 05:08 UTC to 2022 September 29 12:00 UTC and from 2022 September 30 12:52:02 UTC to 2022 October 8 11:17, for a total livetime of ∼837 ks. Level 2 (LV2) data, processed to produce suitable inputs for science analysis, were downloaded from the IXPE archive at HEASARC.[61] One file for each of the three IXPE telescopes was generated, and they were further processed independently. Photons' arrival times are corrected to the solar system barycenter in TDB scale, with the FTOOL/BARYCORR tool, included in HEASOFT 6.31, using the object coordinates stored in the LV2 file, the Jet Propulsion Laboratory Development Ephemeris 421, and the International Celestial Reference System reference frame. Background events in the LV2 files are at first partially rejected. They are identified starting from topological characteristics of the event, e.g., the number of hit pixels and the fraction of the energy in the main track with respect to the total collected for the event. The events falling outside predefined intervals are tagged as background and removed. This approach allows to reduce the background counting rate by more then 30%, at the cost of a reduction of the source count rate by ∼0.5%, which is deemed negligible for the subsequent analysis (see A. Di Marco et al. 2023, in preparation, for a more detailed description).

The source region is then defined with SAOImage Deep Space 9 (DS9; Joye & Mandel 2003) as a circle with radius of 1.′5. The background is extracted from an annulus centered on 1RXS J1708 with inner and outer radii of 2.′5 and 4.′0, respectively. The response to polarization is extracted from LV2 data with the IXPEOBSSIM package (Baldini et al. 2022), which implements the algorithms in Kislat et al. (2015) and is publicly available.[62] The spectro-polarimetric analysis is carried out by feeding the Stokes spectra, generated with the IXPEOBSSIM tool XPBIN, into XSPEC (Arnaud 1996) and exploiting the appropriate response matrices available at HEASARC for modeling the polarization as suggested by Strohmayer (2017). The lightcurve of 1RXS J170849.0-400910 and of the background during the two IXPE observations is shown in Figure 5. Note that the first segment is split in two pointings, the first between 2022 September 19 5:00–7:20 UTC and the second starting at 2022 September 19 17:30 and ending at 2022 September 29 12:00. Both components did not show any indication of either a spectral or polarization variation with time. To test this, we binned the lightcurves of the Stokes parameters and background in bins of 20 ks, and we checked that the variations are compatible with statistical fluctuations only (the null probability for a fit with a constant is acceptable). Therefore, we proceeded with the analysis by summing all the data.

A.2. NICER

In order to complement the IXPE data, we requested a set of new NICER observations, which have been awarded and performed a week after the end of the last IXPE observation. However, all these observations suffered from high optical loading (resulting from a low Sun angle), and thus were unusable for our analysis. We therefore resorted to the use of the NICER archival data, using the most recent available observations (closest in time to the IXPE observation). Specifically, for the contemporaneous spectral fitting with IXPE and Swift spectra, we made use of the observations from 2022 August 21 (observation ID 5593051301).

The data were processed using version 9 of the NICER Data Analysis Software (`NICERDAS`) on version 6.30.1 of `HEASoft`. We applied standard filtering criteria as per the default cuts with `nicerl2`, resulting in 972 s of filtered exposure. The spectrum was then binned with optimal binning (Kaastra & Bleeker 2016) and with a minimum of 25 counts per bin. The background spectrum was generated using version 7 of the 3C50 model (Remillard et al. 2022). The Response Matrix Files (RMFs)and Ancillary Response Files (ARFs) were generated from `nicerrmf` and `nicerarf`, respectively.

A.3. Swift

A Swift-XRT target of opportunity observation was performed on 2022 October 20 for a total of 1020 s in windowed timing mode. The data were processed using the standard HEASoft tools, extracting the spectra using `xselect`, after generating ancillary response file using `xrtmkarf` and the latest calibration files available in the Swift-XRT CALDB. The source was extracted from the cleaned event file using a centered circular region with a radius of 17 pixels. The background region was extracted using an off-centered circular region of the same radius. The extracted source

[61] https://heasarc.gsfc.nasa.gov/docs/ixpe/archive/

[62] https://github.com/lucabaldini/ixpeobssim

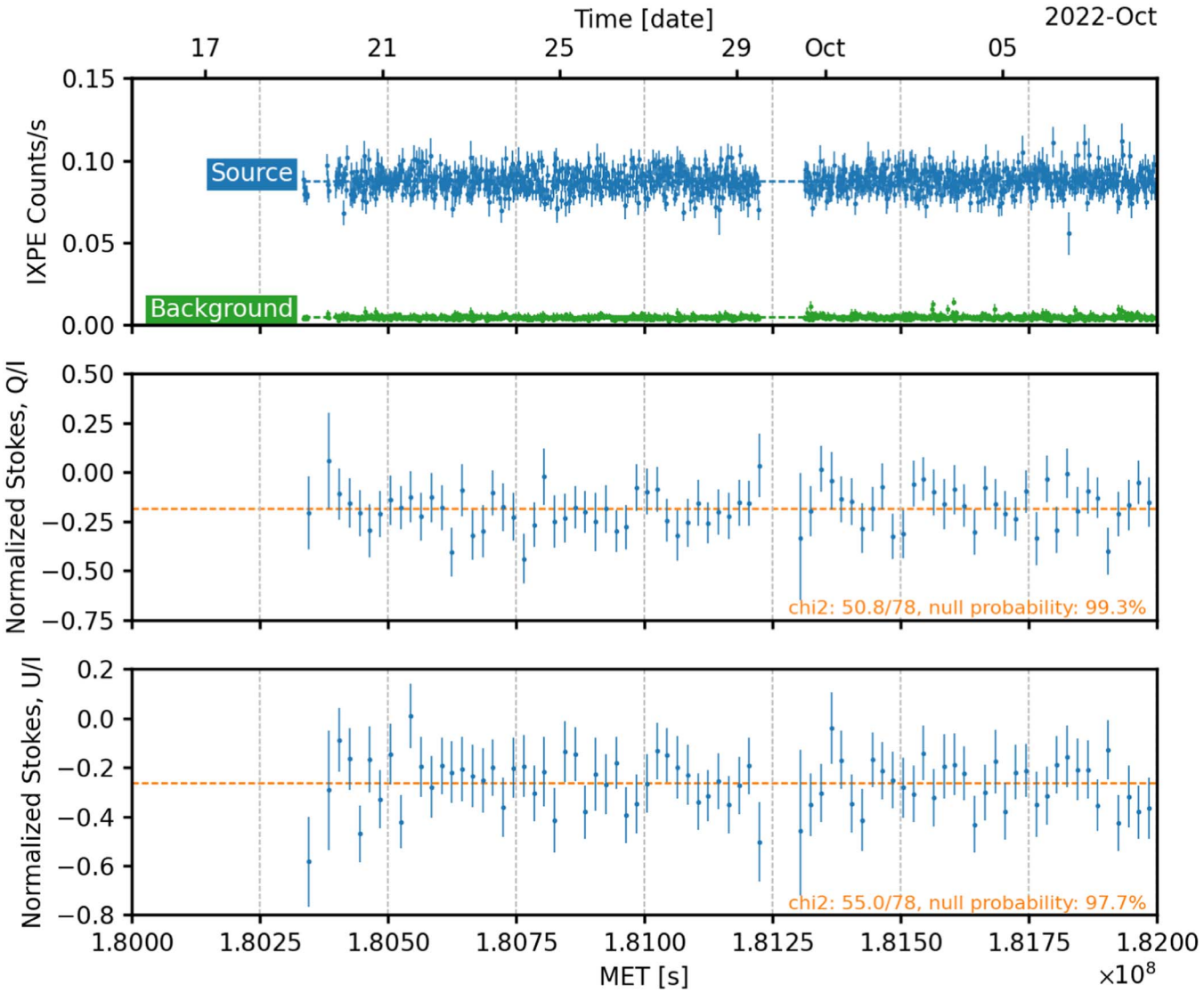

Figure 5. Top panel: 1RXS J1708 lightcurve, averaged over the three IXPE telescopes, for the source and the background. The count rate is averaged over 500 s and integrated over the IXPE nominal energy band, 2.0–8.0 keV. Middle and bottom panels: lightcurve of normalized Stokes parameters; the time bin is 20 ks. In all panels, variations are compatible with statistical fluctuations only: the null probabilty for a fit with a constant is acceptable.

spectra were binned, requiring each spectral channel to have at least 25 counts.

Appendix B
Model Parameters from the Spectro-polarimetric Analysis

As discussed in Section 3, there are two possible spectral decompositions that are both compatible with the data: one consists of a thermal (BB) component plus a nonthermal (PL), and the second consists of two blackbodies. The best fitting model parameters, for the two cases, are listed in Table 2.

Appendix C
Timing Solution

A timing solution of the count rate data has been obtained by following the procedure from Bachetti et al. (2022). We first determined an approximate solution and then used the Pletsch & Clark (2015) maximum likelihood method to refine it. We determined an approximate first solution with the tool `HENzsearch`, running a Z_3^2 search (Buccheri et al. 1983) around the known pulse frequency from Dib & Kaspi (2014). The pulsar was detected with extremely high significance, with $Z_3^2 \sim 16,000$ ($\sim 126\sigma$, considering 10,000 trials), at $f = 0.09079575$ Hz, and $\dot{f} = -2.28 \times 10^{-13}$ Hz s^{-1}. Then, we used the tool `ell1fit`[63] v. 0.2 to run a maximum likelihood fit of the spin solution, using a template for the pulse profile obtained by a Fourier analysis with 4 harmonics, and letting only the spin frequency and its first spin derivative vary. The resulting solution, using epoch MJD 59850.84175 (TDB) as a reference, is $f = 0.090795742(5)$ Hz, $\dot{f} = -1.87(25) \times 10^{-13}$ Hz s^{-1}. The addition of the second frequency derivative did not improve the fit significantly: the 3σ upper limit on the second derivative in our observation is $\sim 2 \times 10^{-19}$ Hz s^{-2}.

ORCID iDs

Silvia Zane https://orcid.org/0000-0001-5326-880X
Roberto Taverna https://orcid.org/0000-0002-1768-618X

[63] https://github.com/matteobachetti/ell1fit

Denis González–Caniulef https://orcid.org/0000-0001-5848-0180
Fabio Muleri https://orcid.org/0000-0003-3331-3794
Roberto Turolla https://orcid.org/0000-0003-3977-8760
Jeremy Heyl https://orcid.org/0000-0001-9739-367X
Keisuke Uchiyama https://orcid.org/0000-0002-7752-9389
Mason Ng https://orcid.org/0000-0002-0940-6563
Toru Tamagawa https://orcid.org/0000-0002-8801-6263
Ilaria Caiazzo https://orcid.org/0000-0002-4770-5388
Niccolò Di Lalla https://orcid.org/0000-0002-7574-1298
Herman L. Marshall https://orcid.org/0000-0002-6492-1293
Matteo Bachetti https://orcid.org/0000-0002-4576-9337
Fabio La Monaca https://orcid.org/0000-0001-8916-4156
Ephraim Gau https://orcid.org/0000-0002-5250-2710
Alessandro Di Marco https://orcid.org/0000-0003-0331-3259
Luca Baldini https://orcid.org/0000-0002-9785-7726
Michela Negro https://orcid.org/0000-0002-6548-5622
Nicola Omodei https://orcid.org/0000-0002-5448-7577
John Rankin https://orcid.org/0000-0002-9774-0560
Giorgio Matt https://orcid.org/0000-0002-2152-0916
George G. Pavlov https://orcid.org/0000-0002-7481-5259
Henric Krawczynski https://orcid.org/0000-0002-1084-6507
Ruth Kelly https://orcid.org/0000-0002-5004-3573
Iván Agudo https://orcid.org/0000-0002-3777-6182
Lucio A. Antonelli https://orcid.org/0000-0002-5037-9034
Wayne H. Baumgartner https://orcid.org/0000-0002-5106-0463
Ronaldo Bellazzini https://orcid.org/0000-0002-2469-7063
Stefano Bianchi https://orcid.org/0000-0002-4622-4240
Stephen D. Bongiorno https://orcid.org/0000-0002-0901-2097
Raffaella Bonino https://orcid.org/0000-0002-4264-1215
Alessandro Brez https://orcid.org/0000-0002-9460-1821
Niccolò Bucciantini https://orcid.org/0000-0002-8848-1392
Fiamma Capitanio https://orcid.org/0000-0002-6384-3027
Simone Castellano https://orcid.org/0000-0003-1111-4292
Elisabetta Cavazzuti https://orcid.org/0000-0001-7150-9638
Chieng-Ting Chen https://orcid.org/0000-0002-4945-5079
Stefano Ciprini https://orcid.org/0000-0002-0712-2479
Enrico Costa https://orcid.org/0000-0003-4925-8523
Alessandra De Rosa https://orcid.org/0000-0001-5668-6863
Ettore Del Monte https://orcid.org/0000-0002-3013-6334
Laura Di Gesu https://orcid.org/0000-0002-5614-5028
Immacolata Donnarumma https://orcid.org/0000-0002-4700-4549
Victor Doroshenko https://orcid.org/0000-0001-8162-1105
Michal Dovčiak https://orcid.org/0000-0003-0079-1239
Steven R. Ehlert https://orcid.org/0000-0003-4420-2838
Teruaki Enoto https://orcid.org/0000-0003-1244-3100
Yuri Evangelista https://orcid.org/0000-0001-6096-6710
Sergio Fabiani https://orcid.org/0000-0003-1533-0283
Riccardo Ferrazzoli https://orcid.org/0000-0003-1074-8605
Javier A. Garcia https://orcid.org/0000-0003-3828-2448
Shuichi Gunji https://orcid.org/0000-0002-5881-2445
Wataru Iwakiri https://orcid.org/0000-0002-0207-9010
Svetlana G. Jorstad https://orcid.org/0000-0001-6158-1708
Philip Kaaret https://orcid.org/0000-0002-3638-0637
Vladimir Karas https://orcid.org/0000-0002-5760-0459
Jeffery J. Kolodziejczak https://orcid.org/0000-0002-0110-6136
Luca Latronico https://orcid.org/0000-0002-0984-1856
Ioannis Liodakis https://orcid.org/0000-0001-9200-4006
Simone Maldera https://orcid.org/0000-0002-0698-4421
Alberto Manfreda https://orcid.org/0000-0002-0998-4953
Frédéric Marin https://orcid.org/0000-0003-4952-0835
Andrea Marinucci https://orcid.org/0000-0002-2055-4946
Alan P. Marscher https://orcid.org/0000-0001-7396-3332
Francesco Massaro https://orcid.org/0000-0002-1704-9850
Tsunefumi Mizuno https://orcid.org/0000-0001-7263-0296
C.-Y. Ng https://orcid.org/0000-0002-5847-2612
Stephen L. O'Dell https://orcid.org/0000-0002-1868-8056
Chiara Oppedisano https://orcid.org/0000-0001-6194-4601
Alessandro Papitto https://orcid.org/0000-0001-6289-7413
Abel L. Peirson https://orcid.org/0000-0001-6292-1911
Matteo Perri https://orcid.org/0000-0003-3613-4409
Melissa Pesce-Rollins https://orcid.org/0000-0003-1790-8018
Pierre-Olivier Petrucci https://orcid.org/0000-0001-6061-3480
Maura Pilia https://orcid.org/0000-0001-7397-8091
Andrea Possenti https://orcid.org/0000-0001-5902-3731
Juri Poutanen https://orcid.org/0000-0002-0983-0049
Simonetta Puccetti https://orcid.org/0000-0002-2734-7835
Brian D. Ramsey https://orcid.org/0000-0003-1548-1524
Ajay Ratheesh https://orcid.org/0000-0003-0411-4243
Oliver J. Roberts https://orcid.org/0000-0002-7150-9061
Roger W. Romani https://orcid.org/0000-0001-6711-3286
Carmelo Sgró https://orcid.org/0000-0001-5676-6214
Patrick Slane https://orcid.org/0000-0002-6986-6756
Paolo Soffitta https://orcid.org/0000-0002-7781-4104
Gloria Spandre https://orcid.org/0000-0003-0802-3453
Douglas A. Swartz https://orcid.org/0000-0002-2954-4461
Fabrizio Tavecchio https://orcid.org/0000-0003-0256-0995
Allyn F. Tennant https://orcid.org/0000-0002-9443-6774
Nicholas E. Thomas https://orcid.org/0000-0003-0411-4606
Francesco Tombesi https://orcid.org/0000-0002-6562-8654
Alessio Trois https://orcid.org/0000-0002-3180-6002
Sergey S. Tsygankov https://orcid.org/0000-0002-9679-0793
Jacco Vink https://orcid.org/0000-0002-4708-4219
Martin C. Weisskopf https://orcid.org/0000-0002-5270-4240
Kinwah Wu https://orcid.org/0000-0002-7568-8765
Fei Xie https://orcid.org/0000-0002-0105-5826

References

Anders, E., & Grevesse, N. 1989, GeCoA, 53, 197
Arnaud, K. A. 1996, in ASP Conf. Ser. 101, Astronomical Data Analysis Software and Systems V, ed. G. H. Jacoby & J. Barnes (San Francisco, CA: ASP), 17
Arzoumanian, Z., Gendreau, K. C., Baker, C. L., et al. 2014, Proc. SPIE, 9144, 914420
Bachetti, M., Heida, M., Maccarone, T., et al. 2022, ApJ, 937, 125
Baldini, L., Bucciantini, N., Lalla, N. D., et al. 2022, SoftX, 19, 101194
Buccheri, R., Bennett, K., Bignami, G. F., et al. 1983, A&A, 128, 245
Burrows, D. N., Hill, J. E., Nousek, J. A., et al. 2005, SSRv, 120, 165
Caiazzo, I., Gonzalez-Caniulef, D., Heyl, J., & Fernandez, R. 2022, MNRAS, 514, 5024

Coti Zelati, F., Rea, N., Pons, J. A., Campana, S., & Esposito, P. 2018, MNRAS, 474, 961
Dib, R., & Kaspi, V. M. 2014, ApJ, 784, 37
Duncan, R. C., & Thompson, C. 1992, ApJL, 392, L9
Durant, M., & van Kerkwijk, M. H. 2006, ApJ, 650, 1070
Gonzalez Caniulef, D., Zane, S., Taverna, R., Turolla, R., & Wu, K. 2016, MNRAS, 459, 3585
González-Caniulef, D., Caiazzo, I., & Heyl, J. 2023, MNRAS, 519, 5902
Gonzalez-Caniulef, D., Zane, S., Turolla, R., & Wu, K. 2019, MNRAS, 483, 599
Gotz, D., Rea, N., Israel, G. L., et al. 2007, A&A, 475, 317
Heyl, J. S., & Shaviv, N. J. 2000, MNRAS, 311, 555
Heyl, J. S., & Shaviv, N. J. 2002, PhRvD, 66, 023002
Ho, W. C. G., & Lai, D. 2003, MNRAS, 338, 233
Israel, G. L., Covino, S., Stella, L., et al. 1999, ApJL, 518, L107
Joye, W. A., & Mandel, E. 2003, in ASP Conf. Ser. 295, Astronomical Data Analysis Software and Systems XII, ed. H. E. Payne, R. I. Jedrzejewski, & R. N. Hook (San Francisco, CA: ASP), 489
Kaastra, J. S., & Bleeker, J. A. M. 2016, A&A, 587, A151
Kaspi, V. M., & Beloborodov, A. M. 2017, ARA&A, 55, 261
Kislat, F., Clark, B., Beilicke, M., & Krawczynski, H. 2015, APh, 68, 45
Krawczynski, H., Taverna, R., Turolla, R., Mereghetti, S., & Rigoselli, M. 2022, A&A, 658, A161
Kuiper, L., Hermsen, W., den Hartog, P. R., & Collmar, W. 2006, ApJ, 645, 556
Lloyd, D. A. 2003, arXiv:astro-ph/0303561
Medin, Z., & Lai, D. 2007, MNRAS, 382, 1833
Mori, K., & Ho, W. C. G. 2007, MNRAS, 377, 905
Perna, R., Heyl, J. S., Hernquist, L. E., Juett, A. M., & Chakrabarty, D. 2001, ApJ, 557, 18
Pletsch, H. J., & Clark, C. J. 2015, ApJ, 807, 18
Potekhin, A. Y., Suleimanov, V. F., van Adelsberg, M., & Werner, K. 2012, A&A, 546, A121
Rea, N., & Esposito, P. 2011, High-Energy Emission from Pulsars and their Systems (Berlin: Springer), 247
Rea, N., Israel, G. L., Oosterbroek, T., et al. 2007, Ap&SS, 308, 505
Rea, N., Israel, G. L., Stella, L., et al. 2003, ApJL, 586, L65
Remillard, R. A., Loewenstein, M., Steiner, J. F., et al. 2022, AJ, 163, 130
Strohmayer, T. E. 2017, ApJ, 838, 72
Sugizaki, M., Nagase, F., Torii, K., et al. 1997, PASJ, 49, L25
Taverna, R., Turolla, R., Gonzalez Caniulef, D., et al. 2015, MNRAS, 454, 3254
Taverna, R., Turolla, R., Muleri, F., et al. 2022, Sci, 378, 646
Taverna, R., Turolla, R., Suleimanov, V., Potekhin, A. Y., & Zane, S. 2020, MNRAS, 492, 5057
Thompson, C., & Duncan, R. C. 1993, ApJ, 408, 194
Turolla, R., Zane, S., & Watts, A. L. 2015, RPPh, 78, 116901
van Adelsberg, M., & Perna, R. 2009, MNRAS, 399, 1523
Voges, W., Aschenbach, B., Boller, T., et al. 1999, A&A, 349, 389
Weisskopf, M. C., Soffitta, P., Baldini, L., et al. 2022, JATIS, 8, 1
Wilms, J., Allen, A., & McCray, R. 2000, ApJ, 542, 914
Xie, F., Di Marco, A., La Monaca, F., et al. 2022, Natur, 612, 658
Zane, S., & Turolla, R. 2006, MNRAS, 366, 727